# Large-Scale Production of 119mTe and 119Sb for Radiopharmaceutical Applications

Kevin T. Bennett,[†,∥] Sharon E. Bone,[†,∥] Andrew C. Akin,[†] Eva R. Birnbaum,[†] Anastasia V. Blake,[†,§] Mark Brugh,[†] Scott R. Daly,[§] Jonathan W. Engle,[†,‡] Michael E. Fassbender,[†] Maryline G. Ferrier,[†] Stosh A. Kozimor,*,[†] Laura M. Lilley,[†] Christopher A. Martinez,[†] Veronika Mocko,[†] Francois M. Nortier,[†] Benjamin W. Stein,[†] Sara L. Thiemann,[†] and Christiaan Vermeulen[†]

†Los Alamos National Laboratory, Los Alamos, New Mexico 87545, United States
‡University of Wisconsin, Madison, Wisconsin 53705, United States
§University of Iowa, Iowa City, Iowa 52242-1294, United States

Ⓢ Supporting Information

**ABSTRACT:** Radionuclides find widespread use in medical technologies for treating and diagnosing disease. Among successful and emerging radiotherapeutics, 119Sb has unique potential in targeted therapeutic applications for low-energy electron-emitting isotopes. Unfortunately, developing 119Sb-based drugs has been slow in comparison to other radionuclides, primarily due to limited accessibility. Herein is a production method that overcomes this challenge and expands the available time for large-scale distribution and use. Our approach exploits high flux and fluence from high-energy proton sources to produce longer lived 119mTe. This parent isotope slowly decays to 119Sb, which in turn provides access to 119Sb for longer time periods (in comparison to direct 119Sb production routes). We contribute the target design, irradiation conditions, and a rapid procedure for isolating the 119mTe/119Sb pair. To guide process development and to understand why the procedure was successful, we characterized the Te/Sb separation using Te and Sb K-edge X-ray absorption spectroscopy. The procedure provides low-volume aqueous solutions that have high 119mTe— and consequently 119Sb—specific activity in a chemically pure form. This procedure has been demonstrated at large-scale (production-sized, Ci quantities), and the product has potential to meet stringent Food and Drug Administration requirements for a 119mTe/119Sb active pharmaceutical ingredient.
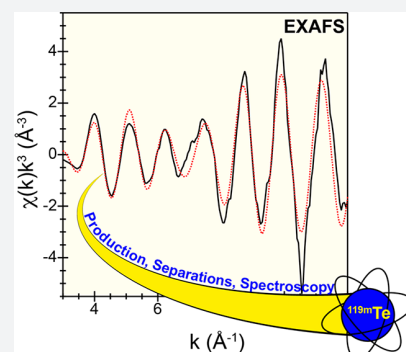
## INTRODUCTION

Recent efforts in using radioactive isotopes *in vivo* have provided creative solutions to numerous global health problems.[1−18] Consider that positron and X-ray emissions from isotopes like 18F, 82Rb, 68Ga, 99mTc, and 201Tl now find widespread use in imaging technologies to treat millions of patients worldwide each year.[19−22] Equally exciting is the potential for harnessing particles emitted during nuclear decay to treat disease, e.g., cancer, bacterial infections, viral infections (like HIV), and other nonmalignant disorders (such as degenerative skeletal pain, Graves orbitopathy, and Gorham Stout syndrome).[23,24] Of numerous radionuclides that show promise, 119Sb is particularly interesting. This isotope decays by emitting K-edge and conversion electrons, collectively called Auger electrons. The 119Sb attraction originates from the low energy (~20 keV) of these Auger electrons, which results in short biological path lengths (~10 μm) that are comparable with the diameter of a many human cells.[25] Hence, therapeutic targeting with 119Sb provides a unique opportunity to deliver a lethal dose of radiation to a targeted diseased cell while leaving the adjacent healthy tissue unharmed.[26−30] The potential for patient recovery along with little to no hematological toxicity

(no negative side-effects) is extraordinary in comparison to nontargeted treatment methods, i.e., nontargeted chemotherapy.

One of the most pragmatic challenges facing implementation of 119Sb in medical applications is associated with access. Today 119Sb can be produced at certain cyclotron facilities in reasonable quantities (0.1−1 Ci).[31,32] Production routes typically involve irradiation of isotopically enriched tin-119 (119Sn) targets (eq 1). Unfortunately, the brisk (relatively short) 119Sb half-life [38.19(22) h][33] and the somewhat complicated and lengthy 119Sn/119Sb separation limit the time interval over which usable activity is available for distribution (Figure 1).

$$^{119}Sn\ (p,n)\ ^{119}Sb \tag{1}$$

Identifying alternative methods that prolong access to 119Sb would expand distribution to medical institutions that do not have colocated 119Sb production facilities. The impact could be dramatic, and transition 119Sb drug development from a niche
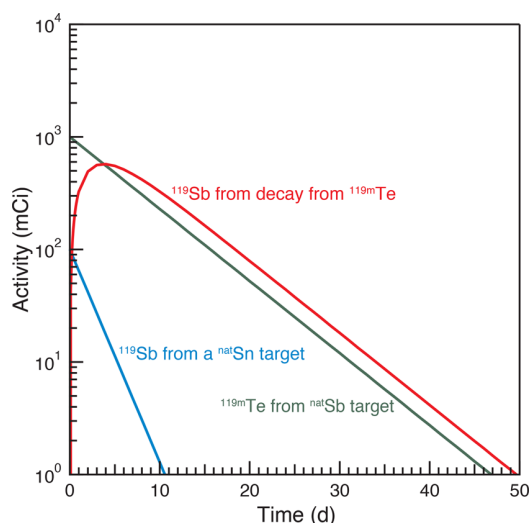
**Figure 1.** Plot showing how $^{119}$Sb isolated from the $^{119m}$Te parent (red and green traces) generated at a high-energy proton source prolongs access time to $^{119}$Sb directly produced from $^{119}$Sn (blue trace) at a common cyclotron.

area of research into a medical therapeutic akin to commercially available Azedra[34] and Xofigo,[35] which use $^{131}$I and $^{223}$Ra as active agents.

Recent nuclear cross-section measurements suggest alternative $^{119}$Sb production routes exist that could prolong access to $^{119}$Sb.[36] These predictions maintain $^{119}$Sb could be made in large quantities (10−100 times larger than the cyclotron-based routes described above) through the nuclear reactions described in eqs 2−4 using high-energy proton sources, i.e., the Isotope Production Facility (IPF) at the Los Alamos Neutron Science Center (LANSCE) at Los Alamos National Laboratory (LANL) and the Brookhaven Linac Isotope Producer (BLIP) at Brookhaven National Laboratory. The proposed approach involves addition of a proton to the two naturally occurring isotopes of Sb, namely, $^{121}$Sb and $^{123}$Sb. Subsequent neutron loss generates $^{119m}$Te, three in the case of $^{121}$Sb and five for $^{123}$Sb. Removal of the $^{nat}$Sb target material leaves behind $^{119m}$Te [$t_{1/2}$ = 4.70(4) days],[33] which slowly decays to the $^{119}$Sb daughter by electron capture, eq 4.

$$^{121}\text{Sb (p,3n)} \ ^{119m}\text{Te} \tag{2}$$

$$^{123}\text{Sb (p,5n)} \ ^{119m}\text{Te} \tag{3}$$

$$^{119m}\text{Te} \xrightarrow{\varepsilon} \ ^{119}\text{Sb} \tag{4}$$

Using $^{nat}$Sb targets to produce $^{119m}$Te (and subsequently $^{119}$Sb) has several advantages over low-energy irradiations of $^{119}$Sn targets that form $^{119}$Sb directly (eq 1). The $^{nat}$Sb targets do not require costly isotopic enrichment; the higher proton energies needed for their irradiation at facilities like IPF and BLIP offer proton fluxes and integrated fluences that are orders of magnitude larger than those used at small cyclotron facilities, and a generator system is possible that uses $^{119m}$Te to make $^{119}$Sb available for weeks from a single production process. Figure 1 demonstrates this graphically by comparing $^{119}$Sb activities generated from two conservative (on the low side of what is possible) production campaigns. One production effort involves cyclotronic irradiation of $^{119}$Sn to directly produce 0.1 Ci of $^{119}$Sb. The other indirectly generates

larger quantities of $^{119}$Sb (1 Ci) through the $^{119m}$Te decay. In these scenarios, small quantities (0.001 Ci) of $^{119}$Sb are available from the $^{119}$Sn route after ∼10 days. In contrast, $^{119}$Sb (0.001 Ci) lingers after ∼45 days when prepared using the $^{119m}$Te/$^{119}$Sb approach, more than 4 times longer than the cyclotron method. Even if $^{119}$Sn production of $^{119}$Sb generated equivalent quantities of $^{119}$Sb to the $^{119m}$Te routes, the $^{119m}$Te approach is still more attractive because the longer $^{119m}$Te decay rate prolongs access to the $^{119}$Sb daughter, eq 4. The combination of "holding-back" $^{119}$Sb by way of its $^{119m}$Te parent and increasing production yields with the (p,3n) and (p,5n) reactions (eqs 2 and 3) offers a technical solution to the "access" problem that plagues $^{119}$Sb drug development.

Herein, we experimentally confirm propositions that the $^{119m}$Te and $^{119}$Sb pair can be generated from $^{nat}$Sb in large quantities by describing a production and separation method that can greatly increase availability. In this manuscript the $^{119m}$Te/$^{119}$Sb production process is described in its entirety, from target design to final product isolation. For example, informed by previous excitation function measurements,[36−40] we established irradiation conditions and an appropriate target that was compatible with large-scale $^{119m}$Te production (Ci-sized quantities). On the separation side, our initial efforts were unsuccessful. They either failed to accommodate the large (25 g) Sb target or were incompatible with the remote handling techniques required to safety manipulate the highly radioactive product. To overcome these challenges, we adopted an unconventional approach in isotope production and made use of X-ray absorption spectroscopy (XAS) to guide efforts that removed Te from Sb. Spectroscopic results informed researchers on differences between Te and Sb in aqueous solutions matrixes and on solid-state chromatographic supports. The information was used to develop a Te/Sb separation procedure that (1) was compatible with large $^{nat}$Sb (25 g) targets, (2) accounted for safety concerns associated with generating large quantities of $^{119m}$Te/$^{119}$Sb, and (3) could be rapidly (∼36 h separation) carried out using remote handling techniques within hot cells.[41] We are most excited by the fact that the final $^{119m}$Te/$^{119}$Sb product could be isolated as a chemically pure sample, in reasonable yield, and with high specific activity. Provided an appropriate $^{119}$Sb generator can be designed that meets strict requirements from the Food and Drug Administration (FDA), this $^{119m}$Te/$^{119}$Sb production route also shows potential for compatibility with active pharmaceutical ingredients (APIs). We hope these results will provide a basis for expanding $^{119}$Sb medical applications and provide researchers insight that supports isotope production and separations for other rare isotopes that show promise in medical applications.

## ■ RESULTS AND DISCUSSION

**Research and Development Approach.** In developing a procedure for separating $^{119m}$Te from $^{nat}$Sb we adopted the unconventional experimental approach of uniting isotope production science with XAS spectroscopy. The goal was to identify experimental conditions under which Te and Sb existed in chemical forms that facilitated separation using chromatographic methods compatible with large-scale processing (25 g Sb, 2.7 Ci or $5.9 \times 10^{16}$ atoms of $^{119m}$Te) and remote handling techniques, i.e., within hot cells. To this end, we used X-ray absorption near edge structure (XANES) to assess oxidation states and extended X-ray absorption fine structure

(EXAFS) to determine local coordination environments for macroscopic amounts (>1 mg) of Te and Sb. This spectroscopic duo revealed differences in charge and chemical forms for Te vs Sb and identified reactions accessible to Te that were inaccessible to Sb. A separation procedure was subsequently developed based on the unique chemical reactivity we observed for Te. To communicate these results most effectively, we first present XANES and EXAFS studies on the aqueous behavior of Te and Sb in solutions that showed promise for the separation (HCl and HF). Next, we describe the developed production method. We conclude by reporting on Te reactivity with three chromatographic resins (CL, Rare Earth, and AG 1-X8) used in the procedure.

**Te and Sb K-Edge XAS Spectroscopy in HCl and HF.**
The Sb oxidation state was characterized as a function of HF concentration. First, a stock solution was obtained by dissolving $Sb^0$ (metal shot) in a mixture of $HNO_3$ (16 M) and HF (28 M). Second, $HNO_3$ was removed and the solution media converted to concentrated HF (28 M). More dilute HF solutions were prepared from this 28 M stock. Oxidation states were determined using Sb K-edge XANES spectroscopy by comparing the inflection point energies from the analytes with oxidation state reference standards, namely, $Sb^V_2O_5$, $Sb^{III}_2O_3$, and $Sb^{III}Cl_3$ (Figures 2 and 3, and see the SI). This approach enabled $Sb^V$ to be distinguished from $Sb^{III}$, as the inflection points for the +5 and +3 oxidation states differed by 3−4 eV (see the SI).[42,43] All spectra obtained from Sb dissolved in HF solutions exhibited inflection points close to 30 495 eV, suggesting that the predominant Sb oxidation state was +5, independent of HF concentration (Figures 2 and 3, and see the SI). Converting the solution matrix to HCl did not appreciably alter the Sb inflection point energies. The highest-energy inflection point observed was in 2 M HCl at 30 496.8(7) eV. Increasing the $Cl^{1-}$ concentration to 12 M systematically decreased the inflection point energy to 30 493.8(7) eV. Although the inflection point energies for Sb in concentrated HCl solutions were ~1 eV lower in energy than $Sb^V_2O_5$, they were still ~2 eV higher in energy than $Sb^{III}Cl_3$ and $Sb^{III}_2O_3$ standards, suggesting that the dominant Sb oxidation state in HCl solutions was also +5.

To characterize chemical identities for primary species present in HCl solutions, shell-by-shell fitting analyses of Sb K-edge EXAFS spectra were performed (Figure 4). When the $Cl^{1-}$ concentration was highest (HCl = 10−12 M), the EXAFS spectra were dominated by a single frequency. This data was best modeled by a shell of 5.8(4) Cl atoms with a 2.370(5) Å Sb−Cl distance (Table 1). Our measured bond distances were shorter than those observed in $K_3Sb^{III}Cl_6$ (ca. 2.52 Å)[44] and $Sb^{III}Cl_2^{1+}$ [2.42(2) Å],[45] which was consistent with the $Sb^V$ oxidation state assignments derived above.[42,43] Hence, we concluded $Sb^VCl_6^{1-}$ was the dominant species present in concentrated HCl matrixes (10−12 M).

Systematically decreasing the $Cl^{1-}$ content—by decreasing HCl concentration—from 8 to 2 M caused a lower-frequency signal to emerge in the Sb EXAFS spectra. This low-frequency contribution was easily observed in the k-space plots of Figure 4. The two oscillations at 6 and 8 Å$^{-1}$ in the 12 M HCl spectrum moved closer together as the $Cl^{1-}$ content decreased until they finally coalesced at 2 M HCl. These low-frequency contributions in k-space gave rise to a peak in the corresponding Fourier transforms at $R + R\delta \sim 1.2$ Å. We fitted this peak using a shell of O atoms. The intensity of this new peak steadily increased with decreasing HCl concentration
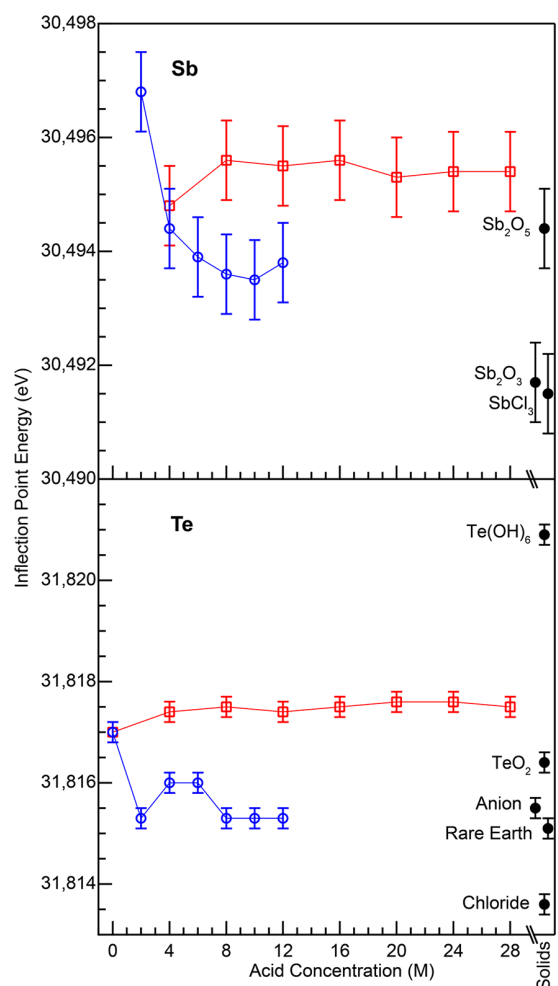


**Figure 2.** Dependence of the inflection point energies on acid concentration from solution phase Sb (top) and Te (bottom) K-edge XANES measurements in HF (red) and HCl (blue) solutions. Measurements from Sb and Te standards and Te that has been loaded onto various resins (anion, Rare Earth, and CL) are shown in black. Uncertainties were estimated at 0.2 eV for Te and 0.7 eV for Sb based on our ability to reproduce these values.

(from 8 to 2 M), such that the O coordination numbers increased from 0.6(4) to 4.8(1.1) while the Cl coordination numbers dropped from 4.8(5) to 1.0(4).

There are multiple ways to interpret these results. One option involved a single $Sb^V$ compound that contained a combination of $Cl^{1-}$, $OH^{1-}$, and $H_2O$ ligands. For example, in 2 M HCl, Sb could exist as $Sb(OH)_4(H_2O)Cl$. Alternatively, a mixture of two $Sb^V$ endmember species—$SbCl_6^{1-}$ in 12 M HCl and $Sb(OH)_5(H_2O)$ in dilute HCl—could be present in 2−8 M HCl. In the latter scenario, the $Sb^V$ speciation in 2 M HCl would contain 15% $SbCl_6^{1-}$ and 85% $Sb(OH)_5(H_2O)$. Increasing the HCl concentration would then systematically increase the percentage of $SbCl_6^{1-}$ and decrease the percentage of $Sb(OH)_5(H_2O)$, (Figure 4). Additional confidence in our interpretation comes from congruency with previous reports showing our proposed dilute endmember $Sb(OH)_5(H_2O)$ exists in aqueous solutions at pH 1.[46] Because EXAFS spectroscopy provides a snapshot of the average Sb coordination environment across all species present in a sample, we could not use this data to distinguish between these
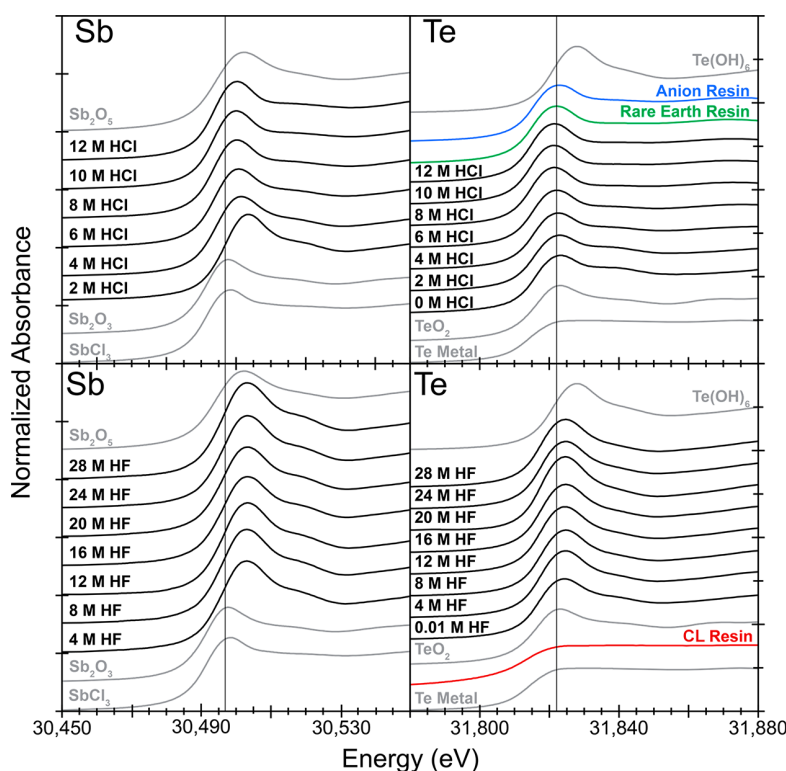
**Figure 3.** Normalized Sb (left) and Te (right) K-edge XANES from aqueous solutions (black traces; top—HCl, 0−12 M; bottom—HF, 0.01−28 M) as well as for Te fixed to the CL (red trace), anion (blue trace), and Rare Earth (green trace) resins. The $SbCl_3$, $Sb_2O_5$, Te metal, $TeO_2$, and $Te(OH)_6$ oxidation state references are shown as gray traces.

two scenarios nor exclude formation of intermediates between the $SbCl_6^{1-}$ and $Sb(OH)_5(H_2O)$ endmembers.[47]

To determine Te oxidation states in relevant aqueous media, a stock solution containing natural-tellurium ($^{nat}Te$) was prepared for XAS analyses. Samples were made by dissolving $Te^0$ (metal shot) in a mixture of HF (28 M) and $HNO_3$ (16 M) followed by $HNO_3$ removal. This stock was used to prepare aqueous $^{nat}Te$ samples with varied HF (0.01−28 M) and HCl (2−12 M) concentrations. Subsequently, Te oxidation states were determined using Te K-edge XANES spectroscopy, as the inflection point energies for $Te^{IV}$ and $Te^{VI}$ typically differ by ~4 eV (Figures 2 and 3, and the SI).[47−49] The 31 817.0(2) eV inflection point measured for $^{nat}Te$ in 0.01 M HF was only 0.6 eV higher in energy than $Te^{IV}O_2$ and substantially lower (by almost 4 eV) in energy than the $Te^{VI}(OH)_6$ standard. Increasing the HF concentration slightly increased the inflection point values by ca. 0.5 eV. Over the entire HF concentration range, the inflection point values averaged 31 817.5 with a standard deviation of only 0.1 eV (1$\sigma$). In HCl, the inflection point energies were lower (by ca. 1.5 eV) relative to Te in straight $H_2O$. These HCl values remained relatively constant over the entire HCl concentration range, averaging 31 815.5(4) eV between 2 and 12 M. Hence, this data suggested $Te^{IV}$ was the predominant species present in all HF (0.01−28 M) and HCl (2−12 M) solutions.

As with Sb, the Te K-edge EXAFS spectra from samples in HCl (0−12 M) were modeled. The Te EXAFS spectra were fitted with inner sphere O and Cl atoms, and the number of O and Cl atoms coordinated to Te varied as a function of $Cl^{1-}$ concentration. At high HCl concentrations (8, 10, 12 M) only Cl atoms were detected: 4.0(4)−4.6(5) Cl atoms with Te−Cl

distances ranging from 2.46(1) to 2.49(1) Å. These distances were consistent with expectation based on ionic radii, i.e., summing the 0.66 four-coordinate $Te^{IV}$ radius with the 1.81 Å $Cl^{1-}$ radius equaled 2.50 Å. Furthermore, our results agreed reasonably well with previous EXAFS measurements made on $Te^{IV}$ in solutions with high Cl concentrations (12 M LiCl and 1 M HCl),[47] which showed 4.3(4) inner sphere $Cl^{1-}$ with a 2.504(5) Å Te−Cl bond distance. Owing to measurement uncertainties (1$\sigma$), $Cl^{1-}$ coordination numbers were bound between 3.6 and 5.1, and we could not rule out the presence of $TeCl_5^{1-}$ and $TeCl_6^{2-}$. Prior UV−vis and Raman spectroscopy studies suggested that the $TeCl_6^{2-}$ species dominated at high HCl concentrations.[50,51]

In contrast, in dilute HCl (0−2 M) no inner sphere $Cl^{1-}$ ligands were detected; only O atoms were observed. The coordination numbers [3.6(3) and 3.2(2)] and Te−O distances [1.89(1) and 1.90(1) Å] were consistent with tellurous acid ($H_3TeO_3^{1+}$) being the major species. This interpretation agreed with previous work by Grundler and co-workers. These authors examined Te speciation in 9.9 M $HClO_4$ solutions (pH < 0) using EXAFS spectroscopy. They found that $H_3TeO_3^{1+}$ was the dominant species with a Te−O bond distance of 1.90(1) Å.[49]

At intermediate HCl concentrations (4 and 6 M), the Te K-edge EXAFS results showed Te coordinated by both O and Cl atoms. The number of coordinated $Cl^{1-}$ ligands increased (and the number of O atoms decreased) with increasing HCl concentration (Table 2). Results from the fitting analyses could indicate that a single Te species existed whose O and Cl coordination numbers systematically varied with HCl concentration (total coordination number of ~4, see Figure 4 and
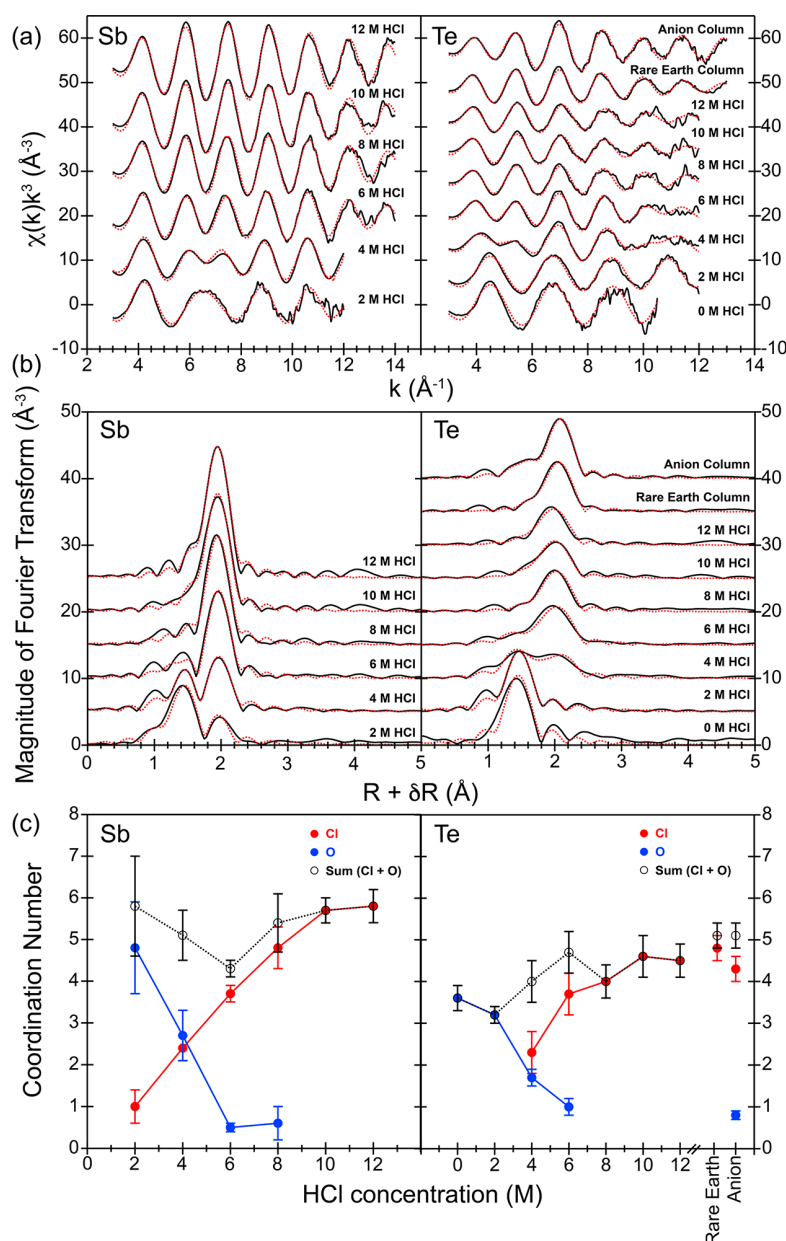
**Figure 4.** Sb and Te K-edge EXAFS (a) and Fourier transform−EXAFS (b) from aqueous solutions (HCl, 0−12 M) as well as from Te fixed to the anion and Rare Earth resins. Experimental spectra are shown in black and fits in red. (c) Graphical representation showing the O (blue ●), Cl (red ●), and the total (○) coordination numbers dependence on HCl concentrations for Sb (left) and Te (right).

Table 2). Alternatively, a mixture of $TeCl_4$ and $H_3TeO_3^{1+}$ could exist in solution, and the ratio of $TeCl_4$ to $H_3TeO_3^{1+}$ would change as a function of HCl content. Another interpretation acknowledges intermediate compounds exist between the high ($TeCl_4$) and the low ($H_3TeO_3^{1+}$) HCl concentration extremes, like $TeCl_4OH^{1-}$ and $TeCl_2(OH)_2$. Again, the composition of the mixture would vary with HCl concentration. The latter interpretation was consistent with Raman and UV−vis data reported previously and suggested mixtures of Te species were present in solutions at moderate HCl concentrations (2.5−8.5 M), including $TeCl_4OH^{1-}$ and $TeCl_2(OH)_2$.[51]

Results from the XAS analyses provided the basis for developing separation strategies for removing $^{119m}Te$ from $^{nat}Sb$ (Scheme 1). Consider, at low HCl concentrations Te

existed primarily as a cationic complex whereas Sb was primarily a neutral compound. At high HCl concentrations a neutral complex dominated the Te speciation, and an anionic complex dominated for Sb. We also surmised that at intermediate HCl concentrations the major Te species in solution involved cationic and neutral compounds, while Sb complexation involved neutral and anionic species. These charge differences provided the opportunity to separate Te from Sb based on ion-exchange chromatography and liquid/liquid extraction schemes.

**Te and Sb Separations.** An $^{nat}Sb$ metal target (25 g; 1.52 in. diameter; 0.136 in. thick) was sealed in an Inconel capsule (window thickness = 0.012 in. per side) designed to withstand high-energy irradiations at the Isotope Production Facility (IPF) at Los Alamos National Laboratory (see the SI). The

498

**Table 1. Fitting Parameters for Sb in Solution with 2−12 M HCl**

| | Sb−Cl | | | |
|---|---|---|---|---|
| sample | $S_0^2$ | CN | $R$ (Å) | $\sigma^2$ (Å²) |
| 2 M HCl | $0.95^a$ | $1.0 \pm 0.4$ | $2.37 \pm 0.018$ | $0.0033^b$ |
| 4 M HCl | 0.95 | $2.4 \pm 0.3$ | $2.39 \pm 0.014$ | 0.0033 |
| 6 M HCl | 0.95 | $3.7 \pm 0.2$ | $2.38 \pm 0.008$ | 0.0033 |
| 8 M HCl | 0.95 | $4.8 \pm 0.5$ | $2.37 \pm 0.008$ | $0.0034 \pm 0.0010$ |
| 10 M HCl | 0.95 | $5.7 \pm 0.3$ | $2.37 \pm 0.005$ | $0.0040 \pm 0.0006$ |
| 12 M HCl | $0.95 \pm 0.06$ | $5.8 \pm 0.4$ | $2.37 \pm 0.005$ | $0.0033 \pm 0.0006$ |
| | Sb−O | | | |
| sample | $S_0^2$ | CN | $R$ (Å) | $\sigma^2$ (Å²) |
| 2 M HCl | 0.95 | $4.8 \pm 1.1$ | $1.94 \pm 0.004$ | $0.0040 \pm 0.0028$ |
| 4 M HCl | 0.95 | $2.7 \pm 0.6$ | $1.95 \pm 0.013$ | $0.0025 \pm 0.0025$ |
| 6 M HCl | 0.95 | $0.5 \pm 0.1$ | $1.96 \pm 0.019$ | $0.0040^c$ |
| 8 M HCl | 0.95 | $0.6 \pm 0.4$ | $1.96 \pm 0.062$ | 0.0040 |
| 10 M HCl | | | | |
| 12 M HCl | | | | |
| sample | $\Delta E$ (eV) | $R$-value | $R$ range (Å) | $k$ range (Å⁻¹) |
| 2 M HCl | $5.05 \pm 2.59$ | 0.028 | 1−2.5 | 3−12 |
| 4 M HCl | $9.35 \pm 1.44$ | 0.012 | 1−2.5 | 3−12 |
| 6 M HCl | $9.90 \pm 1.04$ | 0.016 | 1−2.5 | 3−14 |
| 8 M HCl | $9.36 \pm 1.23$ | 0.015 | 1−2.5 | 3−14 |
| 10 M HCl | $10.04 \pm 0.71$ | 0.008 | 1−2.5 | 3−14 |
| 12 M HCl | $9.99 \pm 0.71$ | 0.008 | 1−2.5 | 3−14 |

$^a$The amplitude reduction factor was set to 0.95 based on previously reported values ($0.95 \pm 0.05$) for $Sb_2O_5$.[46] $^b$The Sb−Cl Debye−Waller factor was constrained based on fits to the 12 M HCl EXAFS spectrum. $^c$The Sb−O Debye−Waller factor was constrained based on fits to the 2 M HCl EXAFS spectrum.

**Scheme 1. Diagram Showing the Average Sb and Te Stoichiometries for Species Present between 0 and 12 M HCl**
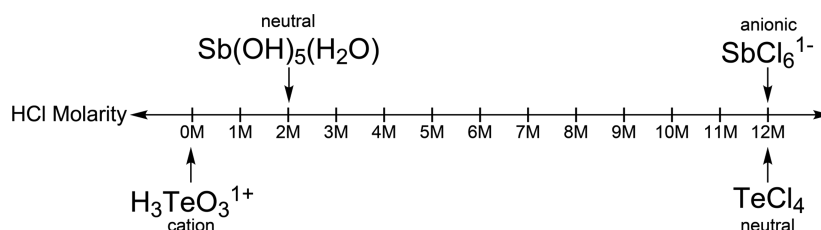


**Scheme 2. Overall Separation Scheme for $^{119m}$Te from an $^{nat}$Sb Target**
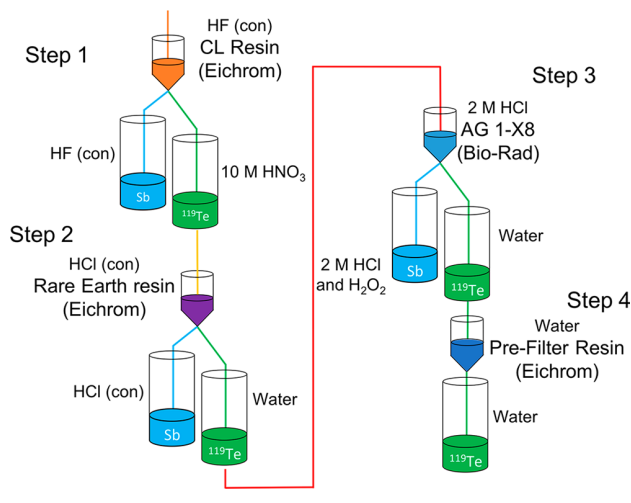


target was irradiated (19.51 h) with an average proton beam current of 100 mA (total charge ca. 1885.4 mA h). Prior to

irradiation, the optimum proton beam energy was determined by irradiating a monitor foil positioned at the target entrance position, the 100 MeV incident beam was then degraded to an average value of 42.5 MeV using precision machined aluminum metal spacers. After irradiation, the target was transferred to a hot cell. Next, the irradiated $^{nat}$Sb (natural isotopic distribution) material was removed from the target shell, and the $^{nat}$Sb metal was dissolved in a mixture of nitric (HNO$_3$, 15.7 M) and hydrofluoric (HF, 28 M) acid for subsequent processing.

Using insight from the Sb and Te K-edge XAS data acquired on aqueous solutions (described above) and solid-state chromatographic resins (described below), the following Te/Sb separation method was developed (Scheme 2). The solution matrix was converted to pure HF in preparation for passage through a column loaded with the commercially available CL resin (Eichrom Technologies). Although this matrix change represented the most time-consuming step in the procedure—accounting for 10 h of the ~36 h process—it was essential for debulking Sb from the $^{119m}$Te analyte. If the solution contained residual HNO$_3$ (from the target dissolution) the separation would fail, and $^{119}$Te would leach through the resin. However, when a pure HF (28 M) solution was

**Table 2. Fitting Parameters for Te in Solution with 0−12 M HCl**

| sample | Te−Cl | | | |
|---|---|---|---|---|
| | $S_0^2$ | CN | R (Å) | $\sigma^2$ (Å²) |
| 0 M HCl | $0.9^a$ | | | |
| 2 M HCl | 0.9 | | | |
| 4 M HCl | 0.9 | 2.3 ± 0.5 | 2.49 ± 0.02 | 0.0058 ± 0.0025 |
| 6 M HCl | 0.9 | 3.7 ± 0.5 | 2.49 ± 0.01 | 0.0067 ± 0.0017 |
| 8 M HCl | 0.9 | 4.0 ± 0.4 | 2.49 ± 0.010 | 0.0075 ± 0.0013 |
| 10 M HCl | 0.9 | 4.6 ± 0.5 | 2.48 ± 0.011 | 0.0097 ± 0.0014 |
| 12 M HCl | 0.9 | 4.5 ± 0.4 | 2.46 ± 0.011 | 0.0098 ± 0.0013 |
| Rare Earth | 0.9 | 4.8 ± 0.3 | 2.51 ± 0.005 | 0.0074 ± 0.0007 |
| Anion | 0.9 | 4.3 ± 0.3 | 2.51 ± 0.006 | 0.0050 ± 0.0008 |

| sample | Te−O | | |
|---|---|---|---|
| | CN | R (Å) | $\sigma^2$ (Å²) |
| 0 M HCl | 3.6 ± 0.3 | 1.89 ± 0.01 | $0.0014^b$ |
| 2 M HCl | 3.2 ± 0.2 | 1.90 ± 0.01 | 0.0014 ± 0.0008 |
| 4 M HCl | 1.7 ± 0.2 | 1.89 ± 0.01 | 0.0014 |
| 6 M HCl | 1.0 ± 0.2 | 1.91 ± 0.02 | 0.0014 |
| 8 M HCl | | | |
| 10 M HCl | | | |
| 12 M HCl | | | |
| Rare Earth | | | |
| Anion | 0.8 ± 0.1 | 1.88 ± 0.01 | 0.0014 |

| sample | $\Delta E$ (eV) | R-value | R range | k range |
|---|---|---|---|---|
| 0 M HCl | 10.64 ± 2.08 | 0.0596 | 1−2.3 | 3−10.5 |
| 2 M HCl | 11.62 ± 1.05 | 0.0114 | 1−3 | 3−12 |
| 4 M HCl | 10.09 ± 1.68 | 0.0388 | 1−3 | 3−12 |
| 6 M HCl | 9.35 ± 1.37 | 0.0295 | 1−3 | 3−12 |
| 8 M HCl | 9.05 ± 0.93 | 0.0206 | 1.2−3 | 3−12 |
| 10 M HCl | 8.04 ± 0.96 | 0.0160 | 1.2−3 | 3−12 |
| 12 M HCl | 7.76 ± 0.86 | 0.0204 | 1.2−3 | 3−12 |
| Rare Earth | 10.10 ± 0.53 | 0.0092 | 1−3 | 3−13 |
| Anion | 10.71 ± 0.78 | 0.0102 | 1−3 | 3−13 |

$^a$Amplitude reduction factor set based on ref 47. $^b$Debye−Waller factor set based on fits of EXAFS spectrum for Te in 2 M HCl.

loaded onto the CL resin bed, a blue band formed at the top of the column; $^{119m}$Te was retained by the resin, and $^{nat}$Sb eluted (Figure 5). Under these conditions, *macroscopic* quantities of the $^{nat}$Sb (demonstrated at 50 g with a mock target) target could be almost completely removed (more than 99.994%) from *microscopic* amounts of $^{119m}$Te (2.69 Ci, 11.5 μg). After the initial separation on CL resin, recovering $^{119m}$Te was not straightforward. It could not be eluted off the column in HF, HCl, or even water. However, in $HNO_3$ (≥10 M) the $^{119m}$Te isotope eluted in near quantitative yield (99%, see the SI). Although this approach successfully accommodated production-scale quantities of $^{nat}$Sb and $^{119m}$Te, it was initially concerning that the CL resin introduced ppm quantities of S and P into the sample. Small-scale experiments used for developing the remote handling methods and the large-scale procedure showed (by ICP-AES) that the $^{119m}$Te eluate contained S and P contamination near 600 and 200 ppm, respectively. Fortunately, we overcame this issue by adding additional S and P removal steps, *vide infra*.

After eluting $^{119m}$Te from the CL resin, the solution matrix was rapidly changed to concentrated HCl (11.7 M) for a second Te/Sb separation. This involved loading the sample onto a Rare Earth resin (Eichrom Technologies) in concentrated HCl. Under these conditions $^{119m}$Te was retained, and $^{nat}$Sb unexpectedly fractionated (Figure 5). Using $^{124}$Sb radiotracers to characterize the Sb elution profile in developmental experiments, we observed approximately half of the $^{124}$Sb was retained on the column, while the rest passed through the column (Figure 5). This $^{nat}$Sb fractionation was of little consequence in terms of $^{119m}$Te recovery because $^{119m}$Te could be eluted cleanly from the Rare Earth resin in $H_2O$, in high yield, and without $^{nat}$Sb contamination. As testament, during developmental experiments using a combination of $^{nat}$Sb (160 mg) and $^{124}$Sb, Sb decontamination factors were unable to be determined as there was neither $^{124}$Sb nor $^{nat}$Sb detected in the $^{119m}$Te elution fractions by γ spectroscopy or
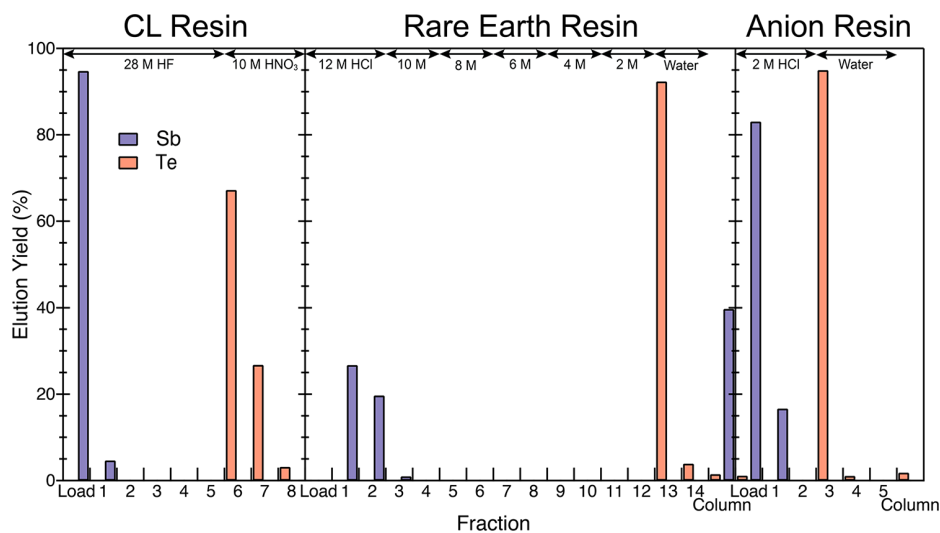


**Figure 5.** Chromatograms from the Te/Sb separations utilizing CL, Rare Earth, and anion-exchange resins. (left) Separation of $^{121}$Te (3240 cps) from stable Sb (160 mg) traced with $^{124}$Sb (114.5 cps) using a Bio-Rad column (10 mL column) containing CL resin (Eichrom Technologies; 1.5 mL; 100−150 μm). (middle) Separation of stable Sb (12 mg), $^{124}$Sb (32 cps), and $^{121m}$Te (260 cps) using a Bio-Rad column (10 mL column) containing Rare Earth resin (Eichrom Technologies; 1.5 mL; 50−100 μm). (right) Separation of stable Sb (12 mg), $^{124}$Sb (32 cps), and $^{121m}$Te (260 cps) using a Bio-Rad column (10 mL) containing AG 1-X8 anion-exchange resin (Bio-Rad; 1.7 mL; 100−200 mesh).

ICP-AES. The $^{119m}$Te yield in these developmental experiments was 97%.

To ensure complete separation of $^{119m}$Te from the $^{nat}$Sb target, we found it prudent to include an anion-exchange-based (AG-1 × 8 resin, Bio-Rad) separation step.[52] Developmental experiments showed this anion-exchange step provided an additional Sb decontamination factor (initial Sb concentration ingoing ÷ final Sb concentration in product) of over 900 (Figure 5). The anion-exchange separation was also attractive because it was fast (5 h), high-yielding ($^{119m}$Te recovery at 97%), and easily incorporated into the large-scale procedure. For example, in the large-scale process, the $^{119m}$Te eluate from the Rare Earth column was acidified with HCl (to 2 M). To ensure high-oxidation states were retained for the analytes in this load solution, peroxide ($H_2O_2$) was added and the solution gently heated. The solution was then loaded onto the anion-exchange resin. Under these conditions $^{nat}$Sb passed directly through the column; $^{119m}$Te was retained, and subsequently eluted with $H_2O$.

The final step in the $^{119m}$Te purification was designed to remove S and P contamination using Prefilter resin (Eichrom Technologies). We observed previously that this resin can significantly decrease organic contaminants in samples.[53,54] Thus, the eluate from the anion-exchange column was loaded directly onto Prefilter resin and $^{119m}$Te eluted. Experiments used for development demonstrated that S and P were removed completely from solutions containing 0.003 and 0.005 mg of S and P, respectively. In these experiments the S and P levels in the eluate were below our limit of detection (~100 ppb for both elements by ICP-AES).

**Te K-Edge XAS Spectroscopy from Columns.** To understand the origin for the chromatographic results described above, a series of Te K-edge XAS measurements were conducted on the first three columns deployed in the separations shown in Scheme 2. In each experiment, macroscopic quantities of naturally occurring tellurium ($^{nat}$Te; ca. 1 mg) were loaded on a resin that was contained in a small column. The entire column was placed in an aluminum holder fixed to a $N_2$(l) cryostat and the XAS spectra collected at low temperature. Given that macroscopic quantities of $^{nat}$Te behaved similarly to microscopic amounts of $^{119}$Te on the three resins we have confidence in correlating spectroscopic results from $^{nat}$Te (macroscopic) with the $^{119}$Te (microscopic) separations.

Analysis of $^{nat}$Te on a CL resin column (used in Step 1 of Scheme 2) provided surprising results. The extractant adsorbed on the CL resin ($R_3P$=S) was not used to directly bind Te$^{IV}$. Instead, the Te K-edge XANES spectrum indicated that Te was retained by the resin as Te$^0$ metal (Figure 3). The inflection point from the resin-retained $^{nat}$Te [31 813.6(3) eV] was nearly identical to that for metallic Te$^0$ at 31 814 eV. These values were ca. 4 eV lower than Te$^{IV}$ in the HF (28 M) load solution (*vide supra*).[55] The spectrum's line shape was also consistent with the spectral features of metallic Te$^0$, in that the absorption peak was substantially attenuated and resembled a simple step function. This interpretation was confirmed by fitting the Te K-edge EXAFS spectrum as metallic Te$^0$ and by subsequent powder X-ray diffraction measurements, which showed diffraction peaks consistent with formation of Te$^0$ on the resin.[56] To the best of our knowledge this represents the first observation of CL resin achieving separations through electron transfer reactions—as opposed to

simple extraction chemistry—and we are currently exploring new potential application of this material.

Similar to the Te K-edge EXAFS results from $^{nat}$Te bound to CL resin, examination of the $^{nat}$Te retained on the Rare Earth resin (Step 2 of Scheme 2) also provided unexpected results. The EXAFS spectrum revealed a single peak, located at approximately the same distance as the peaks in the EXAFS spectra from the 10 and 12 M HCl samples. These similarities suggested that Te was retained by the Rare Earth resin as an anionic chloride complex and showed no evidence of the Rare Earth resin using its octyl(phenyl)-*N,N*-diisobutylcarbamoyl-methylphosphine oxide (CMPO) extractant to form molecular complexes with Te$^{IV}$, like a Te−CMPO compound. Fitting the Rare Earth resin spectrum revealed Te$^{IV}$ coordinated by 4.8(3) Cl atoms at a distance of 2.510(6) Å. This coordination number was slightly higher than that determined for Te$^{IV}$ in 8 M HCl solutions, 4.0(4), and was equivalent within acceptable error to those values determined for the 10 and 12 M HCl solutions (Figure 4). Additionally, the Te−Cl bond distance was slightly longer (by 0.02 Å) for Te$^{IV}$ retained on the Rare Earth resin than Te$^{IV}$ dissolved in 6, 8, 10, and 12 M HCl solutions, which also corresponded well with the increased Cl coordination number. Overall, these results showed the Rare Earth resin acted as a simple anion exchanger under our experimental conditions, and the expected extraction chemistry was not observed.

Interactions between $^{nat}$Te and the anion-exchange resin (AG 1-X8, Bio-Rad) (Step 3, Scheme 2) were also characterized by Te K-edge EXAFS after loading $^{nat}$Te in 2 M HCl onto the resin. The spectroscopic results described above suggested that, when dissolved in 2 M HCl, Te would exist predominantly as a cationic species ($H_3TeO_3^{1+}$). Thus, retention of Te by the anion-exchange resin was perplexing because the resin should only bind anions. Analysis of the anion-exchange resin-retained Te provided insight into the reason for the chromatographic behavior. The dominant peak in the Fourier transformed EXAFS spectrum from retained Te was fitted with Cl atoms and the small shoulder on the main peak fitted with O atoms. The O coordination number was 0.8(1), and the Cl coordination number was 4.3(3). Although the Te−O distance for the sorbed species was equivalent to the HCl solution phase measurements, the Te−Cl bond distance (2.510(6) Å) was slightly longer than the Te−Cl distances in HCl solutions, suggesting that the Te−Cl bond lengthened to accommodate a greater number of ligands in the Te coordination sphere (similar to our observations of the Rare-Earth-retained Te). These results suggested that species with an average stoichiometry of $TeCl_4OH^{1-}$ were retained on the resin. Furthermore, the results indicated that contacting Te$^{IV}$ in 2 M HCl with an anion-exchange resin causes a change in speciation, from $H_3TeO_3^{1+}$ to $TeCl_4OH^{1-}$. Motivated by this observation, we are currently characterizing the complicated reaction chemistry at the anion-exchange resin−HCl mobile phase interface.

## ■ OUTLOOK

The $^{119m}$Te processing method reported here is compatible with performing routine, large-scale production of $^{119m}$Te and $^{119}$Sb (through the decay of the parent isotope $^{119m}$Te). The procedure appropriately accounted for safety concerns associated with the significant radiation doses accompanying large-scale accelerator produced $^{119m}$Te and $^{119}$Sb, in that it could be carried out using remote handling techniques in a hot

cell. Despite these handling challenges, this procedure also enabled $^{119m}$Te and $^{119}$Sb to be isolated rapidly (∼36 h from target dissolution to final product suspension), which is important given the brisk half-lives for $^{119m}$Te [4.70(4) days][33] and $^{119}$Sb [38.19(22) h].[33] The final product was obtained in small volumes of aqueous solution (14 mL), with high specific activities ($^{119m}$Te activity/total mass Te), and in chemically pure forms. No stable Te was detected in the final product by ICP-AES (the minimum detectable concentration in final product was 100 ppb), and the only contaminants observed were phosphorus (5 ppm) and $^{nat}$Sb (2 ppm).

To aid in developing the $^{119m}$Te/$^{119}$Sb production method, significant effort was expended on understanding the separation process. These studies revealed unexpected insight into key separation steps that were responsible for successful $^{119m}$Te processing (Scheme 2). Consider our analyses on the CL resin (Step 1, Scheme 2) used to debulk 99.994% of the 25 g $^{nat}$Sb target material from the $^{119m}$Te product. We assumed initially that the CL resin achieved $^{119m}$Te separation through standard methods, i.e., forming R$_3$P=S—Te bond between $^{119m}$Te and the adsorbed R$_3$P=S extractant. However, the Te K-edge XAS results and powder X-ray diffraction studies showed this was not the case. Instead our results revealed a new reaction pathway available to the CL resin, one that involved an electron transfer reaction to reduce Te$^{IV}$ to Te$^0$. These results demonstrate that CL resin can achieve separations as advertised (by extraction) or unconventionally (observed herein) by acting as a nonconducting stationary support capable of redox chemistry. The impact of this newly observed separation pathway for the CL resin extends beyond processing of $^{119m}$Te, potentially opening doors for additionally innovative solutions to complicated partitioning problems.

Insight into CL resin redox chemistry also explained numerous peculiarities observed during the Te/Sb separation. Prior to the XAS studies, S and P contamination from the CL column was mysterious as was the origin of a blue band that formed on the top of the column. We were additionally confused by observations that HCl, HF, and H$_2$O were ineffective at freeing Te from the CL resin bed because Te$^{IV}$ is quite soluble in these matrixes. Reduction of Te$^{IV}$ to metallic Te$^0$ provided a likely explanation for all of these observations. Redox reactions between the R$_3$P=S extractant on the CL resin and Te$^{IV}$ could introduce P and S decomposition products into the column effluent. Other redox induced decomposition products likely accounted for the blue color on top of the resin. Finally, reduction of Te$^{IV}$ to metallic Te$^0$ explained the unusual elution profile. Metallic Te$^0$ will only elute if dissolved. Contacting the resin with HNO$_3$ (10 M) achieves dissolution, whereas HCl, HF, and H$_2$O do not.

The XAS analysis of retained Te on the Rare Earth (Step 2, Scheme 2) and anion-exchange (Step 3, Scheme 2) resins provided additional insight into the Te/Sb separation procedure. For instance, like the CL resin, we anticipated that the Rare Earth resin would use the adsorbed CMPO extractant to bind Te$^{IV}$. However, this was not observed. Instead, Te K-edge EXAFS spectroscopy showed that TeCl$_5^{1-}$ was retained rather than a Te$^{IV}$—CMPO coordination complex. In hindsight, this observation seemed reasonable as the CMPO extractant was likely protonated in 12 M HCl, leaving the resin to act as a simple anionic ion exchanger.

The AG 1-X8 anion-exchange column provided the only example where a resin deployed in our $^{119m}$Te/$^{119}$Sb process behaved as expected, at least for the most part. For instance,

although anionic exchange partitioning was observed, the results were unexpected based on the aqueous speciation summarized in Scheme 1. The EXAFS analysis of the Te/Sb AG 1-X8 separation was thought-provoking regarding resin performance. We remind the reader that (1) Te$^{IV}$ and Sb$^V$ were loaded onto the AG 1-X8 anion-exchange resin in 2 M HCl, and (2) Te K-edge EXAFS analysis showed that Te existed primary as H$_3$TeO$_3^{1+}$ in 2 M HCl. This cationic species, having no Cl$^{1-}$ and 3.2 ± 0.2 oxygen ligands, should not have been retained by an anion-exchange resin. Indeed, it was not. Instead, the Te$^{IV}$ speciation changed from H$_3$TeO$_3^{1+}$ in the mobile phase to an anionic Te$^{IV}$ species on the resin, with an average stoichiometry of TeCl$_4$OH$^{1-}$. This observation contributes to the growing body of knowledge describing complex—and difficult to characterize—chemistry that occurs at interfaces, e.g., between solids and solutions or between two immiscible liquids.[57−61] We propose two possible pathways that rationalize the Te$^{IV}$ behavior. In the first scenario, the alkyl ammonium (NR$_4^{1+}$) functional group on this solid-state support may force the Cl$^{1-}$ concentration at the surface of the resin bead higher than in the 2 M HCl mobile phase. The increased Cl$^{1-}$ concentration could change the identity of the dominant Te$^{IV}$ species, increase the number of Cl$^{1-}$ ligands bound to Te$^{IV}$, and favor formation of the electrostatically bound TeCl$_4$OH$^{1-}$. The second scenario acknowledges that EXAFS spectroscopy results on the 2 M HCl mobile phase show an average stoichiometry of TeCl$_4$OH$^{1-}$. Other species may be present in small quantities, like TeCl$_4$OH$^{1-}$, TeCl$_5^{1-}$, and TeCl$_6^{2-}$. It seems possible that the positively charged NR$_4^{1+}$ functionalized resin may selectively bind small quantities of TeCl$_4$OH$^{1-}$ (or TeCl$_5^{1-}$/TeCl$_6^{2-}$) present in 2 M HCl, thereby shifting the Te$^{IV}$ speciation at the resin/solution interface. Both scenarios are likely oversimplified. However, these hypotheses were useful in that they provided frameworks to rationalize the retention of Te$^{IV}$ on the anion-exchange resin using the EXAFS data, which unambiguously demonstrates that dominant Te$^{IV}$ species present in the mobile phase were not the major species bound to the solid-state support. We cannot overstate the importance of better characterizing solid−solution interfaces present within separation processes, as the chemical compositions at these assemblages are critical for controlling analyte partitioning. The impact spans beyond that of fundamental curiosity, ranging from fate and transport of toxic ions in the environment, environmental restoration, and (in this case) isotope production for medical purposes.

In summary, the new separation capability for $^{119m}$Te and $^{119}$Sb represents an exciting leap forward for targeted radiotherapeutic use of Auger-emitting isotopes. It offers opportunity to greatly increase access to $^{119}$Sb and expand $^{119}$Sb availability beyond the relatively limited number of medical institutions that have $^{119}$Sb production capabilities. The potential impact of these results is significant, offering opportunity to further explore $^{119}$Sb targeted Auger therapies, to identify appropriate methods for administration (either chelated or nonchelated), and to transition $^{119}$Sb Auger therapy from a niche area of R&D into mainstream medical procedures used to treat disease. The EXAFS results for CL resin performance are also exiting, particularly the revelation that redox reactions can be used to separate Te from Sb. Hence, we are currently trying to expand Te-based electron transfer reactivity to solve challenges in $^{119m}$Te/$^{119}$Sb generator design. The anticipated results have potential to provide a

reliable $^{119}$Sb/$^{119m}$Te generator and further enhance $^{119}$Sb access to researchers and clinicians.

## ■ ASSOCIATED CONTENT

### ⓢ Supporting Information

The Supporting Information is available free of charge on the ACS Publications website at DOI: 10.1021/acscentsci.8b00869.

> Full experimental details including target preparation, target irradiation and opening, dilution, purification, and characterization; and all details associated with the XAS measurements (PDF)

## ■ AUTHOR INFORMATION

### Corresponding Author
*E-mail: stosh@lanl.gov.

### ORCID ⓘ
Kevin T. Bennett: 0000-0002-4320-6733
Sharon E. Bone: 0000-0002-7521-9627
Scott R. Daly: 0000-0001-6229-0822
Maryline G. Ferrier: 0000-0003-0081-279X
Stosh A. Kozimor: 0000-0001-7387-0507

### Author Contributions
$^{\|}$K.T.B. and S.E.B. contributed equally to this manuscript.

### Notes
The authors declare no competing financial interest.

## ■ ACKNOWLEDGMENTS

## ■ REFERENCES

(1) Moretti, J.-L.; Defer, G.; Cinotti, L.; Cesaro, P.; Degos, J.-D.; Vigneron, N.; Ducassou, D.; Holman, B. L. Luxury Perfusion" with 99mTc-HMPAO and 123I-IMP SPECT Imaging during the Subacute Phase of Stroke. *Eur. J. Nucl. Med.* **1990**, *16* (1), 17−22.

(2) Khoo, V. S. Radiotherapeutic Techniques for Prostate Cancer, Dose Escalation and Brachytherapy. *Clin. Oncol.* **2005**, *17* (7), 560−571.

(3) Le, D. Radiopharmaceuticals for Therapy. *J. Nucl. Med.* **2017**, *58* (9), 1526−1526.

(4) Rizzieri, D. Zevalin® (Ibritumomab Tiuxetan): After More than a Decade of Treatment Experience, What Have We Learned? *Crit. Rev. Oncol. Hematol.* **2016**, *105*, 5−17.

(5) Costantini, D. L.; Chan, C.; Cai, Z.; Vallis, K. A.; Reilly, R. M. $^{111}$In-Labeled Trastuzumab (Herceptin) Modified with Nuclear Localization Sequences (NLS): An Auger Electron-Emitting Radiotherapeutic Agent for HER2/Neu-Amplified Breast Cancer. *J. Nucl. Med.* **2007**, *48* (8), 1357−1368.

(6) Quigley, A.-M.; Gnanasegaran, G.; Buscombe, J. R.; Hilson, A. J. W. Technetium-99m-Labelled Sulesomab (LeukoScan) in the Evaluation of Soft Tissue Infections. *Med. Princ. Pract.* **2008**, *17* (6), 447−452.

(7) Reardon, D. A.; Akabani, G.; Coleman, R. E.; Friedman, A. H.; Friedman, H. S.; Herndon, J. E.; Cokgor, I.; McLendon, R. E.; Pegram, C. N.; Provenzale, J. M.; Quinn, J. A.; Rich, J. N.; Regalado, L. V.; Sampson, J. H.; Shafman, T. D.; Wikstrand, C. J.; Wong, T. Z.; Zhao, X.-G.; Zalutsky, M. R.; Bigner, D. D. Phase II Trial of Murine 131 I-Labeled Antitenascin Monoclonal Antibody 81C6 Administered Into Surgically Created Resection Cavities of Patients With Newly Diagnosed Malignant Gliomas. *J. Clin. Oncol.* **2002**, *20* (5), 1389−1397.

(8) Zalutsky, M. R.; Reardon, D. A.; Akabani, G.; Coleman, R. E.; Friedman, A. H.; Friedman, H. S.; McLendon, R. E.; Wong, T. Z.; Bigner, D. D. Clinical Experience with α-Particle Emitting $^{211}$At: Treatment of Recurrent Brain Tumor Patients with $^{211}$At-Labeled Chimeric Antitenascin Monoclonal Antibody 81C6. *J. Nucl. Med.* **2007**, *49* (1), 30−38.

(9) Alvarez-Diez, T. M.; DeKemp, R.; Beanlands, R.; Vincent, J. Manufacture of Strontium-82/Rubidium-82 Generators and Quality Control of Rubidium-82 Chloride for Myocardial Perfusion Imaging in Patients Using Positron Emission Tomography. *Appl. Radiat. Isot.* **1999**, *50* (6), 1015−1023.

(10) Ryo, U. Y.; Vaidya, P. V.; Schneider, A. B.; Bekerman, C.; Pinsky, S. M. Thyroid Imaging Agents: A Comparison of I-123 and Tc-99m Pertechnetate. *Radiology* **1983**, *148* (3), 819−822.

(11) Milenic, D. E.; Brady, E. D.; Brechbiel, M. W. Antibody-Targeted Radiation Cancer Therapy. *Nat. Rev. Drug Discovery* **2004**, *3* (6), 488−499.

(12) Wong, D. F.; Rosenberg, P. B.; Zhou, Y.; Kumar, A.; Raymont, V.; Ravert, H. T.; Dannals, R. F.; Nandi, A.; Brasic, J. R.; Ye, W.; Hilton, J.; Lyketsos, C.; Kung, H. F.; Joshi, A. D.; Skovronsky, D. M.; Pontecorvo, M. J. In Vivo Imaging of Amyloid Deposition in Alzheimer Disease Using the Radioligand $^{18}$F-AV-45 (Flobetapir F 18). *J. Nucl. Med.* **2010**, *51* (6), 913−920.

(13) Kahn, D.; Austin, J. C.; Maguire, R. T.; Miller, S. J.; Gerstbrein, J.; Williams, R. D. A Phase II Study of 90 Y Yttrium-Capromab Pendetide in the Treatment of Men with Prostate Cancer Recurrence Following Radical Prostatectomy. *Cancer Biother.Radiopharm.* **1999**, *14* (2), 99−111.

(14) Scott, A. M.; Wolchok, J. D.; Old, L. J. Antibody Therapy of Cancer. *Nat. Rev. Cancer* **2012**, *12* (4), 278−287.

(15) Djang, D. S. W.; Janssen, M. J. R.; Bohnen, N.; Booij, J.; Henderson, T. A.; Herholz, K.; Minoshima, S.; Rowe, C. C.; Sabri, O.; Seibyl, J.; Van Berckel, B. N. M.; Wanner, M. SNM Practice Guideline for Dopamine Transporter Imaging with 123I-Ioflupane SPECT 1.0. *J. Nucl. Med.* **2012**, *53* (1), 154−163.

(16) Luster, M.; Karges, W.; Zeich, K.; Pauls, S.; Verburg, F. A.; Dralle, H.; Glatting, G.; Buck, A. K.; Solbach, C.; Neumaier, B.; Reske, S. N.; Mottaghy, F. M. Clinical Value of 18F-Fluorodihydroxyphenylalanine Positron Emission Tomography/Computed Tomography (18F-DOPA PET/CT) for Detecting Pheochromocytoma. *Eur. J. Nucl. Med. Mol. Imaging* **2010**, *37* (3), 484−493.

(17) Kung, H. F.; Guo, Y.-Z.; Billings, J.; Xu, X.; Mach, R. H.; Blau, M.; Ackerhalt, R. E. Preparation and Biodistribution of [125I]IBZM: A Potential CNS D-2 Dopamine Receptor Imaging Agent. *Int. J. Radiat. Appl. Instrumentation. Part B. Nucl. Med. Biol.* **1988**, *15* (2), 195−201.

(18) Weldon, M. J.; Joseph, A. E.; French, A.; Saverymuttu, S. H.; Maxwell, J. D. Comparison of 99mTechnetium Hexamethylpropylene-Amine Oxime Labelled Leucocyte with 111-Indium Tropolonate Labelled Granulocyte Scanning and Ultrasound in the Diagnosis of Intra-Abdominal Abscess. *Gut* **1995**, *37* (4), 557−564.

(19) McKillop, J. H. Thallium 201 Scintigraphy. *West J. Med.* **1980**, *133* (1), 26−43.

(20) Nuutila, P.; Raitakari, M.; Laine, H.; Kirvelä, O.; Takala, T.; Utriainen, T.; Mäkimattila, S.; Pitkänen, O. P.; Ruotsalainen, U.; Iida, H.; Knuuti, J.; Yki-Jarvinen, H. Role of Blood Flow in Regulating Insulin-Stimulated Glucose Uptake in Humans. Studies Using Bradykinin, [$^{15}$O]Water, and [$^{18}$F]Fluoro-Deoxy-Glucose and Positron Emission Tomography. *J. Clin. Invest.* **1996**, *97* (7), 1741−1747.

(21) Pagnanelli, R. A.; Basso, D. A. Myocardial Perfusion Imaging with $^{201}$Tl. *J. Nucl. Med. Technol.* **2010**, *38* (1), 1−3.

(22) Schinagl, D. A. X.; Vogel, W. V.; Hoffmann, A. L.; van Dalen, J. A.; Oyen, W. J.; Kaanders, J. H. A. M. Comparison of Five Segmentation Tools for 18F-Fluoro-Deoxy-Glucose−Positron Emission Tomography−Based Target Volume Definition in Head and Neck Cancer. *Int. J. Radiat. Oncol., Biol., Phys.* **2007**, *69* (4), 1282−1289.

(23) Luis, A. M. Radiotherapy for Non-Malignant Diseases. *Reports Pract. Oncol. Radiother.* **2013**, *18*, S14−S15.

(24) Seegenschmiedt, M. H.; Micke, O.; Muecke, R. Radiotherapy for Non-Malignant Disorders: State of the Art and Update of the Evidence-Based Practice Guidelines. *Br. J. Radiol.* **2015**, *88* (1051), 20150080.

(25) Park, S.; Ang, R. R.; Duffy, S. P.; Bazov, J.; Chi, K. N.; Black, P. C.; Ma, H. Morphological Differences between Circulating Tumor Cells from Prostate Cancer Patients and Cultured Prostate Cancer Cells. *PLoS One* **2014**, *9* (1), e85264.

(26) Thisgaard, H.; Jensen, M.; Elema, D. R. Medium to Large Scale Radioisotope Production for Targeted Radiotherapy Using a Small PET Cyclotron. *Appl. Radiat. Isot.* **2011**, *69* (1), 1−7.

(27) Miller, D. A.; Sun, S.; Yi, J. H. Preparation of a $^{118}$Te/$^{118}$Sb Radionuclide Generator. *J. Radioanal. Nucl. Chem.* **1992**, *160* (2), 467−476.

(28) Downs, D.; Miller, D. A. Radiochemical Separation of Antimony and Tellurium in Isotope Production and in Radionuclide Generators. *J. Radioanal. Nucl. Chem.* **2004**, *262* (1), 241−247.

(29) Hassan, K. F.; Spellerberg, S.; Scholten, B.; Saleh, Z. A.; Qaim, S. M. Development of an Ion-Exchange Method for Separation of Radioiodine from Tellurium and Antimony and Its Application to the Production of $^{124}$I via the $^{121}$Sb($\alpha$,n)-Process. *J. Radioanal. Nucl. Chem.* **2014**, *302* (1), 689−694.

(30) Thisgaard, H. Accelerator Based Production of Auger-Electron-Emitting Isotopes for Radionuclide Therapy. Ph.D. Dissertation, Technical University of Denmark, Roskilde, Denmark, 2008.

(31) Thisgaard, H.; Jensen, M. $^{119}$Sb-A Potent Auger Emitter for Targeted Radionuclide Therapy. *Med. Phys.* **2008**, *35* (9), 3839−3846.

(32) Thisgaard, H.; Jensen, M. Production of the Auger Emitter $^{119}$Sb for Targeted Radionuclide Therapy Using a Small PET-Cyclotron. *Appl. Radiat. Isot.* **2009**, *67* (1), 34−38.

(33) Brookhaven National Laboratory, National Nuclear Data Center. http://www.nndc.bnl.gov/chart/ (accessed Dec 30, 2018).

(34) Azedra. https://azedra.com (accessed Oct 18, 2018).

(35) Xofigo. https://www.xofigo-us.com/index.php (accessed Oct 18, 2018).

(36) Mosby, M. A.; Birnbaum, E. R.; Nortier, F. M.; Engle, J. W. Cross Sections for Proton-Induced Reactions on $^{nat}$Sb up to 68 MeV. *Nucl. Instrum. Methods Phys. Res., Sect. B* **2017**, *412*, 34−40.

(37) Takacs, S.; Takacs, M. P.; Hermanne, A.; Tarkanyi, F.; Adam Rebeles, R. Cross Sections of Proton Induced Reactions on $^{nat}$Sb. *Nucl. Instrum. Methods Phys. Res., Sect. B* **2013**, *297*, 44−57.

(38) Takács, S.; Takács, M. P.; Hermanne, A.; Tárkányi, F.; Adam Rebeles, R. Cross Sections of Deuteron-Induced Reactions on $^{nat}$Sb up to 50 MeV. *Nucl. Instrum. Methods Phys. Res., Sect. B* **2012**, *278*, 93−105.

(39) Lagunas-Solar, M. C.; Carvacho, O. F.; Yang, S. T.; Yano, Y. Cyclotron Production of PET Radionuclides: $^{118}$Sb (3.5 min; $\beta^+$ 75%; EC 25%) from High-Energy Protons on Natural Sb Targets. *Appl. Radiat. Isot.* **1990**, *41* (6), 521−529.

(40) Yi, J. H.; Miller, D. A. Cross Sections of $^{nat}$Sb(p,x) Reactions for 30−46 MeV Protons. *Int. J. Radiat. Appl. Instrumentation. Part* **1992**, *43* (9), 1103−1106.

(41) Faßbender, M.; Nortier, F. M.; Phillips, D. R.; Hamilton, V. T.; Heaton, R. C.; Jamriska, D. J.; Kitten, J. J.; Pitt, L. R.; Salazar, L. L.; Valdez, F. O.; Peterson, E. J. Some Nuclear Chemical Aspects of Medical Generator Nuclide Production at the Los Alamos Hot Cell Facility. *Radiochim. Acta* **2004**, *92* (4−6), 237−243.

(42) Fawcett, S. E.; Gordon, R. A.; Jamieson, H. E. Optimizing Experimental Design, Overcoming Challenges, and Gaining Valuable Information from the Sb K-Edge XANES Region. *Am. Mineral.* **2009**, *94* (10), 1377−1387.

(43) Scheinost, A. C.; Rossberg, A.; Vantelon, D.; Xifra, I.; Kretzschmar, R.; Leuz, A.; Funke, H.; Johnson, C. A. Quantitative Antimony Speciation in Shooting-Range Soils by EXAFS Spectroscopy. *Geochim. Cosmochim. Acta* **2006**, *70* (13), 3299−3312.

(44) Martineau, E.; Milne, J. B. The Stereochemistry of Hexachloroantimony(Lll) Compounds. *J. Chem. Soc. A* **1970**, 2971−2974.

(45) Oelkers, E. H.; Sherman, D. M.; Ragnarsdottir, K. V.; Collins, C. An EXAFS Spectroscopic Study of Aqueous Antimony(III)-Chloride Complexation at Temperatures from 25 to 250°C. *Chem. Geol.* **1998**, *151*, 21−27.

(46) Tella, M.; Pokrovski, G. S. Stability and Structure of Pentavalent Antimony Complexes with Aqueous Organic Ligands. *Chem. Geol.* **2012**, *292*−*293*, 57−68.

(47) Etschmann, B. E.; Liu, W.; Pring, A.; Grundler, P. V.; Tooth, B.; Borg, S.; Testemale, D.; Brewe, D.; Brugger, J. The Role of Te(IV) and Bi(III) Chloride Complexes in Hydrothermal Mass Transfer: An X-Ray Absorption Spectroscopic Study. *Chem. Geol.* **2016**, *425*, 37−51.

(48) Grundler, P. V.; Brugger, J.; Meisser, N.; Ansermet, S.; Borg, S.; Etschmann, B.; Testemale, D.; Bolin, T. Xocolatlite, $Ca_2Mn_2^{4+}Te_2O_{12} \bullet H_2O$, a New Tellurate Related to Kuranakhite: Description and Measurement of Te Oxidation State by XANES Spectroscopy. *Am. Mineral.* **2008**, *93* (11−12), 1911−1920.

(49) Grundler, P. V.; Brugger, J.; Etschmann, B. E.; Helm, L.; Liu, W.; Spry, P. G.; Tian, Y.; Testemale, D.; Pring, A. Speciation of Aqueous Tellurium(IV) in Hydrothermal Solutions and Vapors, and the Role of Oxidized Tellurium Species in Te Transport and Gold Deposition. *Geochim. Cosmochim. Acta* **2013**, *120*, 298−325.

(50) Baker, L.; Taylor, M. J. Raman and $^{125}$Te NMR Spectroscopic Evidence on the Solvent Extraction of Tellurium (IV) Species from HCl Solutions. *J. Raman Spectrosc.* **1994**, *25*, 845−847.

(51) Milne, J. B. Hexachlorotellurate(IV) Hydrolysis Equilibria in Hydrochloric Acid. Measurement by Raman and $^{125}$Te NMR Spectroscopy and a Reconsideration of Earlier Spectrophotometric Results. *Can. J. Chem.* **1991**, *69* (6), 987−992.

(52) Saito, N. Selected Data on Ion Exchange Separations in Radioanalytical Chemistry. *Pure Appl. Chem.* **1984**, *56* (4), 523−539.

(53) Ferrier, M. G.; Stein, B. W.; Bone, S. E.; Cary, S. K.; Ditter, A. S.; Kozimor, S. A.; Lezama Pacheco, J. S.; Mocko, V.; Seidler, G. T. The Coordination Chemistry of Cm$^{III}$, Am$^{III}$, and Ac$^{III}$ in Nitrate Solutions: An Actinide L$_3$-Edge EXAFS Study. *Chem. Sci.* **2018**, *9*, 7078−7090.

(54) Ferrier, M. G.; Stein, B. W.; Batista, E. R.; Berg, J. M.; Birnbaum, E. R.; Engle, J. W.; John, K. D.; Kozimor, S. A.; Lezama Pacheco, J. S.; Redman, L. N. Synthesis and Characterization of the Actinium Aquo Ion. *ACS Cent. Sci.* **2017**, *3* (3), 176−185.

(55) Thompson, A.; Attwood, D.; Gullikson, E.; Howells, M.; Kim, K.-J.; Kirz, J.; Kortright, J.; Lindau, I.; Liu, Y.; Pianetta, P.; Robinson, A.; Scofield, J.; Underwood, J.; Williams, G.; Winick, H. *X-Ray Data Booklet*, 3rd ed.; Lawrence Berkley National Laboratory: Berkley, CA, 2009.

(56) Kawakita, Y.; Yao, M.; Endo, H. Short and Long Bonds in Liquid Tellurium. *J. Non-Cryst. Solids* **1999**, *250–252*, 447–452.

(57) Darab, J. G.; Amonette, A. B.; Burke, D. S. D.; Orr, R. D.; Ponder, S. M.; Schrick, B.; Mallouk, T. E.; Lukens, W. W.; Caulder, D. L.; Shuh, D. K. Removal of Pertechnetate from Simulated Nuclear Waste Streams Using Supported Zerovalent Iron. *Chem. Mater.* **2007**, *19* (23), 5703–5713.

(58) Saslow, S. A.; Um, W.; Pearce, C. I.; Engelhard, M. H.; Bowden, M. E.; Lukens, W.; Leavy, I. I.; Riley, B. J.; Kim, D.-S.; Schweiger, M. J.; Kruger, A. A. Reduction and Simultaneous Removal of $^{99}$Tc and Cr by $Fe(OH)_2$(s) Mineral Transformation. *Environ. Sci. Technol.* **2017**, *51* (15), 8635–8642.

(59) Luksic, S. A.; Kim, D. S.; Um, W.; Wang, G.; Schweiger, M. J.; Soderquist, C. Z.; Lukens, W.; Kruger, A. A. Effect of Technetium-99 Sources on Its Retention in Low Activity Waste Glass. *J. Nucl. Mater.* **2018**, *503*, 235–244.

(60) Ozkanlar, A.; Kelley, M.; Clark, A. Water Organization and Dynamics on Mineral Surfaces Interrogated by Graph Theoretical Analyses of Intermolecular Chemical Networks. *Minerals* **2014**, *4* (1), 118–129.

(61) Rydberg, J., Cox, M., Musikas, C., Choppin, G. R., Eds. *Solvent Extraction Principles and Practice*, 2nd ed.; Marcel Dekker Inc.: New York, 2004.